

Numerical renormalization group approach to fluctuation exchange in the presence of electron-phonon coupling: Pairing in the Holstein–Hubbard model

C.-H. Pao

Department of Physics, National Chung Cheng University,

Chia-Yi, 621 Taiwan, R.O.C.

H.-B. Schüttler

Center for Simulational Physics, Department of Physics & Astronomy,

University of Georgia, Athens, GA 30602

(February 7, 2008)

Abstract

The fluctuation exchange (FLEX) approximation is applied to study the Holstein–Hubbard model. Due to the retarded nature of the phonon-mediated electron-electron interaction, neither fast Fourier transform (FFT) nor previously developed NRG methods for Hubbard-type purely electronic models are applicable, while brute force solutions are limited by the demands on computational time and storage which increase rapidly at low temperature T . Here, we describe a new numerical renormalization group (NRG) technique to solve the FLEX equations efficiently. Several orders of magnitude of CPU time and storage can be saved at low T ($\sim 80K$). To test our approach, we compare our NRG results to brute force calculations on small lattices at elevated temperatures. Both s -wave and d -wave superconducting phase diagrams are then obtained by applying the NRG approach at low T . The isotope effect for s -wave pairing is BCS-like in a realistic phonon frequency

range, but vanishes at unphysically large phonon frequency (\sim band width). For d -wave pairing, the isotope exponent is negative and small compared to the typical observed values in non-optimally doped cuprates.

I. INTRODUCTION

A large body of experimental evidence suggests that several high- T_c cuprate superconductors exhibit a pairing state of $d_{x^2-y^2}$ symmetry^{1,2}. In combination with the large superconducting transition temperature of these materials, this suggests a superconducting pairing mechanism of predominantly electronic origin. In particular anti-ferromagnetic (AF) spin fluctuation (SF) exchange has been proposed as a possible electronic candidate mechanism^{3–8} which would tend to give rise to $d_{x^2-y^2}$ pairing symmetry.

However, except near certain “optimal” doping concentrations, many cuprates exhibit a quite noticeable doping dependent isotope effect^{9–12} and other pronounced, superconductivity-related lattice effects¹³. This indicates that electron-phonon (EP) interactions could be important and should be included in the theory.^{14,15}

In the past decade, conserving self-consistent field (SCF) methods¹⁶ and related diagrammatic approaches, such as the fluctuation exchange (FLEX) approximation^{4,5,17–22} have been used to study AF SF exchange within the framework of microscopic correlated electron models. Most of the FLEX-based SCF studies so far have been limited to Hubbard-type models with instantaneous, local Coulomb interactions in simple tight-binding models, and some extensions to long-range Coulomb interactions^{23,24}. For these types of model systems, both numerical renormalization group (NRG)¹⁹ and fast Fourier transform (FFT)¹⁷ methods have been developed and successfully applied to solve the FLEX equations efficiently on large space-time lattices in the physically relevant low-temperature regime. The numerical solution of the FLEX equations is greatly simplified in instantaneous interaction models, due to the fact that the bare electron-electron interaction potential is frequency independent.

When EP interactions are introduced into the model, already the bare electron-electron potential becomes explicitly frequency dependent, due the retarded nature of the phonon-mediated interaction. In that case, the solution of the FLEX equations requires the inversion of certain, large fermion frequency matrices which, in a brute force approach, would increase the demands on CPU time and memory consumption by several orders of magnitude, relative

to the purely electronic models studied so far. Also, neither FFT approaches¹⁷ nor the original form of the NRG method¹⁹ can be used here to reduce the numerical effort to manageable proportions.

Previous SCF studies of strongly correlated electron models with EP coupling²⁵ have included renormalization of the Coulomb and phonon-mediated potential at the level of an RPA particle-hole bubble. In this much simpler approach, one neglects the electron–electron exchange scattering which arises in the full FLEX approximation, due to the Pauli exclusion principle. This simpler RPA-based approximation²⁵ then avoids the frequency matrix inversion problem, since the latter arises only from the exchange ladder diagrams. This may be a good approximation when the Coulomb repulsion is strongly screened and the phonon frequency is small. These are, essentially, the conditions under which Migdal’s theorem is valid²⁶ and the Eliashberg theory^{27–29} of phonon-mediated conventional superconductivity is applicable. In general, these conditions may not be satisfied in correlated electron systems and it may be necessary to include both Coulomb and EP contributions to the electron exchange vertex.

In the present paper, we describe an extension of the NRG approach which will allow us to incorporate EP interactions into a Hubbard-type correlated electron model and handle the resulting frequency matrix inversions in the FLEX equations efficiently. An efficient algorithm to solve this matrix inversion problem in the present context is also an important first step towards studying the next level of SCF theory, such as, for example, the parquet theory^{5,30,31}. Our present treatment is limited to the case of the so-called Holstein-Hubbard model^{25,32,33} where the phonon-mediated electron-electron potential is without momentum dependence. However, when combined with recently developed real-space basis representation approaches,^{23,24,34} our basic method to the frequency matrix inversion problem will also become applicable to bare potentials which are frequency *and* momentum dependent.

Preliminary results obtained with our present frequency matrix NRG technique for the *d*-wave instability of the Holstein-Hubbard model have been reported elsewhere³⁵. The purpose of the present paper is to give a first detailed account of the technique itself, to

present results for the *s*-wave instability and for the competition between *d*- and *s*-wave pairing in their respective parameter regimes.

The paper is organized as follows: in Section II, we summarize the FLEX approximation for the Holstein–Hubbard model and define the notations used in the paper. In Section III, we describe our fermion frequency matrix NRG technique in detail. In Section IV, we present our results obtained with the NRG approach for the Holstein–Hubbard model. They include a comparison of results for one-particle correlation functions obtained with the NRG and, respectively, by the brute force approach; and some applications to the superconducting instabilities and the isotope effect of the Holstein–Hubbard model. We conclude with a brief summary in Section V.

II. HOLSTEIN–HUBBARD MODEL IN THE FLEX APPROXIMATION

We start from the simplest microscopic model, including both an on-site Hubbard U Coulomb repulsion and a local Holstein-type EP coupling to an Einstein phonon branch, The Hamiltonian of this Holstein–Hubbard model^{25,32,33} can be written as:

$$H = -t \sum_{\langle ij \rangle \sigma} \left[c_{i\sigma}^\dagger c_{j\sigma} + H.C. \right] - \mu \sum_{i\sigma} n_{i\sigma} + U \sum_i n_{i\uparrow} n_{i\downarrow} \\ + \sum_i \left[\frac{p_i^2}{2M} + \frac{1}{2} K u_i^2 \right] - C \sum_{i\sigma} u_i \left(n_{i\sigma} - \frac{1}{2} \right), \quad (1)$$

with a nearest neighbor hopping t , chemical potential μ , on-site Coulomb repulsion U , on-site EP coupling constant C , harmonic restoring force constant K , and ionic oscillator mass M . The $c_{i\sigma}^\dagger$ ($c_{i\sigma}$) is the electron creation (annihilation) operator at site i and spin σ ; $n_{i\sigma}$ is the number operator; and u_i is the local ionic displacement at lattice site i and $p_i = -i\hbar\partial/\partial u_i$. The dispersionless bare phonon frequency is

$$\Omega_p = (K/M)^{1/2} \quad (2)$$

and the phonon-mediated on-site attraction is

$$U_p = C^2/K. \quad (3)$$

The bare interaction vertices entering into the FLEX treatment are shown in Fig.1, including the particle-hole density and magnetic vertices [Figs. 1(b) and 1(c)]

$$V_{n_1,n_2,n_3,n_4}^D(i\nu_m) = v_{n_1,n_4}^D(i\nu_m)\delta_{n_1,n_2+m}\delta_{n_3+m,n_4} , \quad (4)$$

where

$$v_{n_1,n_4}^D(i\nu_m) = 2v_p(i\nu_m) - v_p(i\omega_{n_1} - i\omega_{n_4}) + U \quad (5)$$

and

$$V_{n_1,n_2,n_3,n_4}^M(i\nu_m) = v_{n_1,n_4}^M(i\nu_m)\delta_{n_1,n_2+m}\delta_{n_3+m,n_4} , \quad (6)$$

where

$$v_{n_1,n_4}^M(i\nu_m) = -[v_p(i\omega_{n_1} - i\omega_{n_4}) + U] , \quad (7)$$

and the particle-particle singlet and triplet vertices [Fig. 1(d)]

$$V_{n_1,n_2,n_3,n_4}^S(i\nu_m) = v_{n_1,n_4}^S(i\nu_m)\delta_{n_1,-n_2+m}\delta_{-n_3+m,n_4} , \quad (8)$$

where

$$v_{n_1,n_4}^S(i\nu_m) = \frac{1}{2}[v_p(i\omega_{n_1} - i\omega_{n_4}) + v_p(i\omega_{n_1} + i\omega_{n_4} - i\nu_m) + 2U] \quad (9)$$

and

$$V_{n_1,n_2,n_3,n_4}^T(i\nu_m) = v_{n_1,n_4}^T(i\nu_m)\delta_{n_1,-n_2+m}\delta_{-n_3+m,n_4} \quad (10)$$

where

$$v_{n_1,n_4}^T(i\nu_m) = \frac{1}{2}[v_p(i\omega_{n_1} - i\omega_{n_4}) - v_p(i\omega_{n_1} + i\omega_{n_4} - i\nu_m)] . \quad (11)$$

Here, the electron-electron potential includes both the Hubbard U and the phonon-mediated contribution [Fig. 1(a)]

$$v_p(i\nu_m) = -U_p\Omega_p^2/(\Omega_p^2 + \nu_m^2) . \quad (12)$$

The boson Matsubara frequencies are denoted by $\nu_m = 2m\pi T$ and the fermion Matsubara frequencies by $\omega_n = (2n + 1)\pi T$ with integer m and n .

In the FLEX approximation, the single-particle self-energy is then given by⁴

$$\begin{aligned} \Sigma(k) = \sum_{\mathbf{k}', i\omega_n'} \frac{T}{N} & \left\{ \left[V_2(k - k'; i\omega_n) + V^{ph}(k - k'; i\omega_n) \right] G(k') \right. \\ & \left. + V^{pp}(k - k'; i\omega_n) G^*(k') \right\} \end{aligned} \quad (13)$$

where the effective interaction potentials are given by⁴

$$\begin{aligned} V_2(q; i\omega_n) = -v_p(i\nu_m) & + \\ \sum_{i\omega_{n''}} [v_p(i\nu_m) + U] & [2v_p(i\nu_m) - v_p(i\omega_n - i\omega_{n''} - i\nu_m) + U] \bar{\chi}_{ph}(q; i\omega_{n''}) , \end{aligned} \quad (14)$$

$$\begin{aligned} V^{ph}(q; i\omega_n) = \sum_{i\omega_{n''}} \left\{ \frac{1}{2} [D(1 + D)^{-1} - D]_{n,n''}(q) v_{n'',n}^D(i\nu_m) + \right. \\ \left. \frac{3}{2} [M(1 + M)^{-1} - M]_{n,n''}(q) v_{n'',n}^M(i\nu_m) \right\} , \end{aligned} \quad (15)$$

$$\begin{aligned} V^{pp}(q; i\omega_n) = - \sum_{i\omega_{n''}} \left\{ [S(1 + S)^{-1} - S]_{n,n''}(q) v_{n'',n}^S(i\nu_m) + \right. \\ \left. 3[T(1 + T)^{-1} - T]_{n,n''}(q) v_{n'',n}^T(i\nu_m) \right\} , \end{aligned} \quad (16)$$

$$R_{n,n''}(q) = v_{n,n''}^R(i\nu_m) \quad \begin{cases} \bar{\chi}_{ph}(q; i\omega_{n''}) & \text{for } R = D \text{ or } M , \\ \bar{\chi}_{pp}(q; i\omega_{n''}) & \text{for } R = S \text{ or } T . \end{cases} \quad (17)$$

Here, we are using a momentum-energy vector notation where, for fermion lines, $k \equiv (\mathbf{k}, i\omega_n)$ and $k' \equiv (\mathbf{k}', i\omega_{n'})$ and, for boson lines, $q \equiv (\mathbf{q}, i\nu_m)$. The Green's function is

$$G(k) = [i\omega_n - \epsilon_{\mathbf{k}} - \Sigma(k)]^{-1} , \quad (18)$$

and the tight binding band

$$\epsilon_{\mathbf{k}} = -2t(\cos \mathbf{k}_x + \cos \mathbf{k}_y) - \mu . \quad (19)$$

The bare particle-hole and particle-particle fluctuation functions are then defined as:

$$\bar{\chi}_{ph}(q; i\omega_n) = -\frac{T}{N} \sum_{\mathbf{k}} G(k + q) G(k) , \quad (20)$$

$$\bar{\chi}_{pp}(q; i\omega_n) = \frac{T}{N} \sum_{\mathbf{k}} G(k + q) G(-k) , \quad (21)$$

without summation over the fermion Matsubara frequency $i\omega_n$.

Eqs. (13–21) are solved iteratively. The iteration proceeds as follows: (1) choose the temperature and either a fixed electron concentration $\langle n \rangle$ or a fixed chemical potential μ ; (2) guess an initial self-energy $\Sigma(k)$ at this temperature and electron concentration, *e.g.*, $\Sigma \equiv 0$; (3) calculate the Green's function $G(k)$ from Eq. (18); (4) calculate the bare particle-hole and particle-particle fluctuation functions by equations (20) and (21) using the Green's function obtained in step (3); (5) evaluate the matrices R in all four channels and the effective potentials V_2 , V^{ph} , and V^{pp} ; (6) update the self-energy by Eq. (13); (7) using the updated self-energy Σ from step (6) as input, go back to step (3) to calculate an updated Green's function G . The iterative cycle, consisting of steps (3) through (7), is then repeated until a converged self-energy is obtained. If $\langle n \rangle$ is to be fixed to a given input value, then the chemical potential μ must be adjusted accordingly during the self-consistent calculation.

Because of the retarded nature of $v_p(i\nu_m)$ the bare vertices in Fig.1(b-d) depend explicitly on the internal frequency transfer. As a consequence, a frequency matrix inversion is necessary to evaluate the fluctuation potentials, V^{ph} and V^{pp} , in Eqs. (15) and (16). In a brute force approach, this matrix dimension can become as large as 500^2 to 1000^2 (the size of the entire fermion Matsubara frequency set) near the transition temperature. Furthermore, for each iteration, the number of such matrix inversions to be carried out is about the same as the number of boson Matsubara frequencies times the size of the momentum grid. At the space-time lattice sizes required to study the physically interesting low-temperature regime, it is therefore not possible to carry out such a brute force calculation with currently available computing resources. Recent FFT and numerical NRG techniques, developed for the pure Hubbard FLEX equations are also not directly applicable. In the next section, we will describe a generalized “fermion frequency matrix” NRG method to handle the numerics efficiently.

After a convergent self-energy is obtained at a fixed temperature and electron filling, the search for pairing instabilities requires the calculation of the maximal eigenvalue of the

pairing kernel, $\lambda(T)$, as a function of temperature T , from

$$\lambda(T)\phi(k) = -\frac{T}{N} \sum_{\mathbf{k}', i\omega_n'} V_{\text{pair}}(k, k'; T) G(k') G(-k') \phi(k') , \quad (22)$$

where the pairing potential V_{pair} is⁴:

$$V_{\text{pair}}(k, k'; T) = \frac{1}{2}v_p(i\omega_n - i\omega_{n'}) - \frac{1}{2}[D(1+D)^{-1}]_{n,n'}(k - k') v_{n',-n}^D(k - k') \\ + \frac{3}{2}[M(1+M)^{-1}]_{n,n'}(k - k') v_{n',-n}^M(k - k') . \quad (23)$$

The instability is reached when $\lambda(T)$ approaches unity, *i.e.*,

$$\lambda(T) \rightarrow 1 \Rightarrow T \rightarrow T_c . \quad (24)$$

III. NUMERICAL RENORMALIZATION GROUP APPROACH FOR THE HOLSTEIN–HUBBARD MODEL

A numerical NRG method has been successfully applied to the FLEX equations of the Hubbard model¹⁹, which has a frequency- and momentum-indepedent bare interaction, the on-site Coulomb U . In this case the matrix inversion in equations (15) and (16) can be carried out analytically and the NRG operations are greatly simplified¹⁹. Due to the frequency dependence of the phonon-mediated interaction v_p , we now have to construct a more general NRG operation in which the frequency dependence of the bare interaction is taken into account. The detailed procedure will now be described.

The NRG evaluation of the self-energy follows closely the original NRG approach described in Ref. 19. We will largely adopt the notation and terminology introduced therein. We are implementing a pure “frequency NRG” (in the sense of Ref. 19). That is, the grid of momentum points \mathbf{k} is chosen from the outset to be dense enough for the lowest temperatures to be reached and remains constant throughout all NRG steps; only the Matsubara frequency grids ($i\omega_n, i\nu_m$) change from one NRG step to the next.

The basic assumption underlying the NRG approach is that

(1) quantities such as the $\Sigma(k)$ and $G(k)$ are, to good approximation, independent of temperature at high frequencies, $|i\omega_n| \gg T$ and

(2) within that high-frequency regime, they are slowly varying with $i\omega_n$, on ω_n -scales of order T and that

(3) the contribution to $\Sigma(k)$ arising from scattering into the high frequency region [$|i\omega_{n'}| \gg T$ in Eq. (13)], denoted by $\Delta\Sigma(k)$ below, is to good approximation independent of temperature and slowly varying for *all* $i\omega_n$.

For the case of the pure Hubbard model, these NRG assumptions have been verified in great detail, by explicit numerical calculations¹⁹. A general justification of these assumptions can be given. It is based on the notion that the energy denominators in the Green's function $G(k)$ become very large and essentially T -independent for $|i\omega| \gg T$. Hence, all strongly T -dependent details are “washed out” in the high-frequency regime¹⁹.

As a consequence, only the low-frequency part of Σ , for $|i\omega_n| \lesssim T$, arising from scattering into the low-frequency region $|i\omega_{n'}| \lesssim T$ in Eq. (13), exhibits substantial T -dependence. As described in Ref. 19, one therefore divides the self-energy $\Sigma(k)$ in Eq. (13) into two contributions, arising respectively from the scattering $i\omega_n \rightarrow i\omega_{n'}$ into a “low” region L [i.e. $i\omega_{n'} \in L$ in equation (13)] and into a “high” region [$i\omega_{n'} \in H$ in equation (13)], that is,

$$\Sigma(k) = \frac{T}{N} \sum_{\mathbf{k}'} \sum_{i\omega_{n'} \in L} S_\Sigma(k, k') + \Delta\Sigma(k). \quad (25)$$

Here $S_\Sigma(k, k')$ denotes the summand in Eq. (13), and $\Delta\Sigma$ is the contribution from the $i\omega_{n'}$ -summation over the “high” region H .

The basic idea of the NRG approach is to reduce the numerical effort by evaluating $\Delta\Sigma(k)$ at a higher temperature, on a correspondingly coarser Matsubara grid. This higher- T result is then interpolated onto the finer Matsubara grid relevant to the lower T . The interpolation onto the lower- T Matsubara grid needs to be performed only for Matsubara frequencies $i\omega_n \in L$. Only the “low” contribution in Eq. (25) needs to be evaluated by summing $i\omega_{n'}$ over the L -portion of the finer, lower- T grid and this, again, needs to be done only for $i\omega_n \in L$.

Starting from a large initial temperature T_0 and large initial Matsubara summation cut-off Ω_0 , this basic NRG step is carried out repeatedly, through a sequence of decreasing temperatures

$$T_0 > T_1 > \dots > T_i > \dots \quad (26)$$

and decreasing Matsubara cut-offs

$$\Omega_0 > \Omega_1 > \dots > \Omega_i > \dots , \quad (27)$$

until the desired final temperature is reached. The initial maximal cutoff must be chosen large enough that the physical results of the calculation, $\Sigma(k; T)$ and $\lambda(T)$, are independent of Ω_0 , *i.e.*, typically large compared to the bandwidth $8t$.

The subsequent renormalized Ω_i (with $i > 0$) delineate the boundaries between the low and high regions, L_i and H_i , in the i -th NRG step where

$$L_i = \{i\omega_n^{(i)} \mid \Omega_i > |\omega_n^{(i)}|; n \text{ integer}\} \quad (28)$$

and

$$H_i = \bigcup_{j=1}^i \Delta H_j \quad (29)$$

comprises the high-frequency region increments ΔH_j of the present ($j = i$) and all prior ($j < i$) NRG steps, given by

$$\Delta H_j = \{i\omega_n^{(j-1)} \mid \Omega_{j-1} > |\omega_n^{(j-1)}| > \Omega_j; n \text{ integer}\} \quad (30)$$

The respective fermion Matsubara frequency grids are given by

$$i\omega_n^{(j)} = (2n+1)\pi T_j . \quad (31)$$

for integer n and j . In order to ensure that the summands in Eq. (35) below enter with the correct weights, the Ω_j and T_j are chosen to obey the grid matching conditions

$$\Omega_j = 2\pi N_j T_j, \quad \Omega_j = 2\pi K_j T_{j-1} \quad (32)$$

so that

$$T_j/T_{j-1} = K_j/N_j, \quad \Omega_j/\Omega_{j-1} = K_j/N_{j-1} \quad (33)$$

with N_j and K_j integer and $K_j \geq N_j \geq 1$, as described in detail in Ref. 19. The calculations presented below are based on a “factor-2” renormalization group with $\Omega_j/\Omega_{j-1} = T_j/T_{j-1} = 1/2$, as illustrated by the frequency grids shown in Fig. 2. Note that the resulting NRG fermion Matsubara grid $L_i \cup H_i$ at temperature T_i is substantially “diluted” compared to the full, dense Matsubara grid

$$A_i = \{i\omega_n^{(i)} \mid \Omega_0 > |\omega_n^{(i)}|; n \text{ integer}\}. \quad (34)$$

The latter constitutes the basic frequency summation domain in a “brute force” calculation at temperature T_i .

The contribution from the H_i region, $\Delta\Sigma^{(i)}(k)$, is “frozen in” during the self-consistency iteration at temperature T_i . It is calculated, prior to the self-consistency iteration, by

$$\Delta\Sigma^{(i)}(k) = \sum_{j=0}^{i-1} \frac{T_j}{T_i} \sum_{\mathbf{k}'} \sum_{i\omega_{n'}^{(j)} \in \Delta H_{j+1}} S_{\Sigma}^{(j)}(k, k') \quad (35)$$

$$= \Delta\Sigma^{(i-1)} + \frac{T_{i-1}}{T_i} \sum_{\mathbf{k}'} \sum_{i\omega_{n'}^{(i-1)} \in \Delta H_i} S_{\Sigma}^{(i-1)}(k, k') \quad (36)$$

$$\equiv \Delta\Sigma^{(i-1)} + \delta\Sigma^{(i)}, \quad (37)$$

where now $k' \equiv (\mathbf{k}', i\omega_{n'}^{(j)})$ and $S_{\Sigma}^{(j)}(k, k')$ is the summand in Eq. (13), computed with the Green’s function $G^{(j)}(k')$, which, in turn, is obtained via the Dyson equation (18) from the self-energy $\Sigma^{(j)}(k')$ on the grid $L_j \cup H_j$ at temperature T_j . Note here that the linear interpolation of the summand from higher- to lower- T frequency grids introduces the temperature re-weighting factor T_j/T_i into the summation in Eq. (35).

The evaluation of the increment $\delta\Sigma^{(i)}$ via Eq. (37) needs to be carried out only for $i\omega$ -points in L_{i-1} . Both $\delta\Sigma^{(i)}$ and $\Sigma^{(i-1)}$ are then added and interpolated onto the finer $i\omega_n^{(i)}$ -grid, inside L_i , to obtain $\Delta\Sigma^{(i)}$ on L_i . This fixed $\Delta\Sigma^{(i)}$ is then used in the (re-)calculation of $\Sigma^{(i)}$ on L_i , via Eq. (25), during the self-consistency iteration at temperature T_i .

Note that $\Delta\Sigma^{(i)}(\mathbf{k}, i\omega_n^{(j)})$ does *not* have to be calculated or stored for grid points outside of the low-frequency domain L_i , that is, for $i\omega_n^{(j)} \in H_i$. The values of $\Sigma^{(i)}(\mathbf{k}, i\omega_n^{(j)})$ on H_i are already “frozen in” before the self-consistency iteration at temperature T_i , since, by the above-stated NRG assumption of T -independence in H_i ,

$$\Sigma^{(i)}(\mathbf{k}, i\omega_n^{(j)}) = \Sigma^{(i-1)}(\mathbf{k}, i\omega_n^{(j)}) = \dots = \Sigma^{(j)}(\mathbf{k}, i\omega_n^{(j)}) \quad (38)$$

for $i > j$ and $i\omega_n^{(j)} \in H_i$. Hence, the values of $\Sigma^{(j)}$ on $H_j \subset H_i$ become “frozen in” (*i.e.*, permanently stored) after the j -th NRG step, and need not be re-calculated during subsequent NRG steps $i > j$. Only the values of $\Sigma^{(i)}$ on the low-frequency grid L_i need to be re-calculated and iterated to self-consistency during the i -th NRG step.

In order to evaluate the self-energy Σ , we therefore need the effective potentials V_2 , V^{ph} and V^{pp} at $i\omega_n$ and $i\omega_{n'}$ in the L -region only. However, the fermion frequency summation over $i\omega_{n''}$ and the fermion frequency matrix inversions in equations (15) and (16) still run over the whole Matsubara frequency range up to the cutoff Ω_0 . We therefore have to develop an efficient algorithm to overcome the fast growth of CPU time and memory requirements associated with these matrix operations at low temperatures. To this end, the NRG approach, outlined above for the self-energy $\Sigma(k)$, must be extended to the fermion frequency matrices, $R_{n,n'}(q)$, where R stands for D , M , S , or T , as defined in Eq. (17). In the following, we will, for simplicity, omit the q -argument and use the notation

$$R(i\omega_n, i\omega_{n'}) \equiv R(i\omega_n, i\omega_{n'}; q) \equiv R_{n,n'}(q) . \quad (39)$$

As defined in Eqs. (17–21), these R -matrix elements can be regarded as the values of an analytical function $R(i\omega, i\omega')$, defined for continuous $i\omega$ - and $i\omega'$ -arguments. The basic assumption underlying our NRG approach for the R -matrix is that $\frac{1}{T}R(i\omega, i\omega')$, as defined in Eqs. (17)–(21) is

- (1) independent of temperature and
- (2) slowly varying on an $i\omega$ -scale of order T ,

if *either* $|i\omega| \gg T$ *or* $|i\omega'| \gg T$ *or* both. The justification for these assumptions lies again

in the high-frequency behavior of the energy denominators of the Green's function $G(k)$, analogous to the NRG assumptions for the self-energy. We can therefore use the same strategy as in the NRG approach for the self-energy:

We again divide the full Matsubara frequency range into an L - and an H -region and, in the H -region, we calculate the R -matrix at a higher temperature on a correspondingly coarser grid. For all required Matsubara frequency summations in the H -region, the R -matrix is then, again, interpolated onto the finer grid. In detail, this works as follows:

The full R -matrix, denoted by $R^{(i)}$ at temperature T_i , is defined for matrix indices $i\omega_n^{(i)}$ covering the full, dense $i\omega_n^{(i)}$ -grid A_i , Eq. (34), up to the maximum cutoff Ω_0 . In all matrix multiplications during the i -th NRG step, the full $R^{(i)}$ is now replaced by a “diluted” R -matrix, which needs to be evaluated and stored only for indices on the NRG frequency grid $L_i \cup H_i$. Those matrix elements which are eliminated by this procedure from the full R -matrix are approximated by appropriate inter- and extrapolations from the $R^{(i)}$ -matrix elements retained.

Consider, for example, a typical matrix-vector multiplication of the R -matrix with a fermion frequency vector $f(i\omega)$. At the i -th NRG step, the required summation over all Matsubara frequency matrix indices $i\omega_n^{(i)}$ up to the cutoff, $|\omega_n^{(i)}| < \Omega_0$, is replaced by summations over the “diluted” frequency grid $L_i \cup H_i$. That is, rather than carrying out the matrix-vector multiplication on the full, dense A_i -grid to obtain

$$g(i\omega_n^{(i)}) \equiv \sum_{i\omega_{n'}^{(i)} \in A_i} R^{(i)}(i\omega_n^{(i)}, i\omega_{n'}^{(i)}) f(i\omega_{n'}^{(i)}) , \quad (40)$$

we evaluate instead $g(i\omega_n^{(j)})$ on the NRG grid $i\omega_n^{(j)} \in L_i \cup H_i$ by linear interpolation of the summand in the H_i -region, which yields, similar to Eq. (35),

$$\begin{aligned} g(i\omega_n^{(j)}) = & \sum_{i\omega_{n'}^{(i)} \in L_i} R^{(i)}(i\omega_n^{(j)}, i\omega_{n'}^{(i)}) f(i\omega_{n'}^{(i)}) \\ & + \sum_{j'=0}^{i-1} \sum_{i\omega_{n'}^{(j')} \in \Delta H_{j'+1}} \frac{T_{j'}}{T_i} R^{(i)}(i\omega_n^{(j)}, i\omega_{n'}^{(j')}) f(i\omega_{n'}^{(j')}) \end{aligned}$$

$$= \sum_{i\omega_n^{(j')} \in L_i \cup H_i} \frac{T_{j'}}{T_i} R^{(i)}(i\omega_n^{(j)}, i\omega_n^{(j')}) f(i\omega_n^{(j')}). \quad (41)$$

Note that the interpolation again introduces a temperature re-weighting factor $T_{j'}/T_i$ into the summation over the coarsened grid. The values of $g(i\omega_n^{(i)})$ and $f(i\omega_n^{(i)})$ on the original full A_i -grid are then again representable by interpolation in terms of the $g(i\omega_n^{(j)})$ - and $f(i\omega_n^{(j)})$ -values, respectively, on the NRG grid $L_i \cup H_i$.

This NRG grid representation of the R -matrix, Eq. (41), is also used to carry out the matrix inversion of $Q \equiv 1 + R$ entering into Eqs. (15) and (16). From Eq. (41) it is easy to see that, at the i -th NRG step, the problem is reduced to carrying out the matrix inversion of a “diluted” Q -matrix with matrix elements

$$Q^{(i)}(i\omega_n^{(j)}, i\omega_n^{(j')}) = \delta_{n,n'} \delta_{j,j'} + \frac{T_{j'}}{T_i} R^{(i)}(i\omega_n^{(j)}, i\omega_n^{(j')}), \quad (42)$$

where the matrix indices $i\omega_n^{(j)}, i\omega_n^{(j')}$ are restricted to the NRG grid $L_i \cup H_i$.

Based on the above-stated NRG assumption of approximate T -independence of R/T in the high-frequency region, we can express the $R^{(i)}$ matrix elements in the “ $H_i - H_i$ ” region by R -matrix elements already calculated in previous NRG steps. That is, analogous to Eq. (38), we have

$$R^{(i)}(i\omega_n^{(j)}, i\omega_n^{(j')}) = \frac{T_i}{T_{i-1}} R^{(i-1)}(i\omega_n^{(j)}, i\omega_n^{(j')}) = \dots = \frac{T_i}{T_{j''}} R^{(j'')}(i\omega_n^{(j)}, i\omega_n^{(j')}) \quad (43)$$

if both $i\omega_n^{(j)}$ and $i\omega_n^{(j')} \in H_i$. Here j'' denotes the larger of j and j' . In other words, after the j -th NRG step, the $H_j - H_j$ matrix elements of $R^{(j)}$ are “frozen in” and need not be recalculated in subsequent NRG steps $i > j$, except for a change in the temperature prefactor. Only those matrix elements of $R^{(i)}$ connecting L_i to H_i and L_i to L_i need to be calculated and updated to self-consistency during the self-consistency iteration of the i -th NRG step.

In the pairing eigenvalue calculation, Eq. (22), we can use the same interpolative approach described above for the R -matrix, to carry out matrix multiplications with the pairing kernel, exploiting the diluted, but non-equidistant NRG frequency grid $L_i \cup H_i$ at the final

temperature $T = T_i$. The non-equidistant nature of the grid will again introduce temperature re-weighting factors into the Matsubara summation, analogous to Eq. (41).

The dimension of $Q^{(i)}$ on the NRG grid $L_i \cup H_i$ is $\mathcal{N}(L_i \cup H_i) \times \mathcal{N}(L_i \cup H_i)$ where $\mathcal{N}(L_i \cup H_i)$ denotes the total number of grid points in $L_i \cup H_i$. The inversion of $Q^{(i)}$ at all momentum-energy-transfer vectors q [see Eqs. (15–17)] is by far the most CPU time consumptive step at low temperatures. In, say, a “factor-2” NRG calculation, $\mathcal{N}(L_i \cup H_i)$ at low temperatures increases with $1/T$ as $\log_2(\frac{1}{\pi}\Omega_0/T)$; the amount of CPU time for inversion of a general $D \times D$ matrix scales as D^3 ; there are of order $N_\omega \times N \times N_{\text{it}}$ such matrix inversions [one per q -vector and self-consistency iteration] in each NRG step, where N is the spatial lattice ($\equiv \mathbf{k}$ grid) size, $N_\omega = \Omega_0/(\pi T)$ is the size of the original Matsubara frequency grid for maximal cutoff Ω_0 and final temperature T , and N_{it} is a typical number of self-consistency iterations needed per NRG step; and the number of NRG steps to reach the final temperature T scales as $\log_2(\frac{1}{\pi}\Omega_0/T)$. The total CPU time of the full NRG low- T self-energy calculation therefore scales as $N_{\text{it}} \times N \times (\frac{1}{\pi}\Omega_0/T) \times [\log_2(\frac{1}{\pi}\Omega_0/T)]^4$. This should be compared to the CPU time of a brute force calculation which, estimated along similar lines, scales at least as $N_{\text{it}} \times N \times (\frac{1}{\pi}\Omega_0/T)^4$. The savings in CPU time of the NRG approach relative to a brute force calculation is therefore a factor of order $(\frac{1}{\pi}\Omega_0/T)^3 / [\log_2(\frac{1}{\pi}\Omega_0/T)]^4$.

The memory requirements for both NRG and brute force method are dominated by the storage of the $R^{(i)}$ - and $Q^{(i)}$ -matrices. Following the foregoing dimensionality estimates, this scales as $N \times (\frac{1}{\pi}\Omega_0/T) \times [\log_2(\frac{1}{\pi}\Omega_0/T)]^2$ in the NRG and as $N \times (\frac{1}{\pi}\Omega_0/T)^3$ in the brute force approach. Thus, in terms of memory consumption, the NRG saves a factor of order $(\frac{1}{\pi}\Omega_0/T)^2 / [\log_2(\frac{1}{\pi}\Omega_0/T)]^2$ relative to the brute force approach.

IV. RESULTS

To begin with, we explore the frequency and temperature dependence of the self-energy and Green’s function of the pure Holstein model ($U = 0$) in Fig. 3, using a brute force calculation for temperatures $T/t = 1.0, 0.5, 0.25$, and 0.125 . We use a maximum cutoff

frequency $\Omega_0/t = 25$, a 16^2 momentum grid, and an electron concentration $\langle n \rangle = 1.0$. In Fig. 3(a) and (b), we plot the real part and imaginary part of the self-energy, respectively, as a function of Matsubara frequency at $\mathbf{k} = (1.77, 1.77)$, which is a point just above the Fermi surface along the diagonal direction. As expected in the high frequency region, the temperature dependence of the self-energy is much smaller than in the low frequency region. Note that we plot the imaginary part of as Σ_2/ω_n instead of Σ_2/t , which emphasizes the low- $i\omega$ region at low temperature.

Fig. 3(c) shows the Green's function at these parameters. It is quite clear that the high temperature behavior of the one-particle function is “frozen in” very quickly as the temperature decreases. As explained in the previous section, this is very important for the fermion frequency matrix NRG method to be applicable, since fluctuation propagators in the effective or pairing potentials, Eqs. (14-16) and (23), are calculated from the one-particle Green's function. Clearly, at high frequencies the Green's function can be interpolated by the high temperature results without loosing any informations.

At Fig. 4, we plot the self-energy and Green's function right at the Fermi surface for $\mathbf{k} = (2.95, 0.20)$. At half-filling, the real parts of self-energy and of Green's function vanish at the Fermi surface, due to particle-hole symmetry. The low frequency behavior becomes much sharper at the Fermi surface, but the high frequency parts of Σ_2 and G_2 are almost temperature independent.

In order to test the accuracy of our NRG approach, we use the factor-2 frequency NRG operation with constant $N_j = 4$ and $K_j = 8$, starting at $T_0/t = 1.0$, as described in the previous section. After three such NRG operation, we thus reach the final $T \equiv T_3 = 0.125t$. We plot the self-energy and Green's function for two different momentum points in Fig. 5, for $\mathbf{k} = (1.77, 1.77)$, and in Fig. 6, for $\mathbf{k} = (2.95, 0.20)$. For comparison, we show the brute force results obtained for the same model parameters, temperature T , and Matsubara cutoff $\Omega_0 = 25.13$ (fixed). There is remarkable agreement between the two methods. However, the NRG grid L_i , Eq. (28), to be summed over in the self-consistency iterations, contains only $2N_i = 8$ fermion Matsubara frequencies at each NRG step i , down to $T = T_3 = 0.125$

and $\Omega_3 = 3.1$. By contrast, in the brute force approach one has to sum over the full, dense A_i -grid, Eq. (34), with $\Omega_0/(\pi T) = 64$ fermion Matsubara frequencies. In table I, we list the memory and CPU time per iteration for both approaches. Savings of memory and CPU time of about two orders of magnitude are achieved by the NRG approach, without significant loss in accuracy.

Next, we examine the stability of the NRG results against changes in the NRG control parameters and NRG protocol. Fig. 7 shows the s -wave eigenvalue calculation for three different “lower cutoff” frequencies $\Omega_\ell/t = 12.57, 6.283$, and 3.142 , which correspond to carrying out a total of, respectively, $\ell = 3, 4$, and 5 factor-2 NRG steps, each starting from $T_0/t = 4.0$ and $\Omega_0/t = 100.5$, with fixed $N_0 = N_1 = \dots = N_\ell = 4$. In each of these three calculations, the ℓ -th factor-2 NRG step is followed by one “fixed-cutoff” step where the cutoff, $\Omega_{\ell+1}$, is left unchanged at $\Omega_{\ell+1} = \Omega_\ell$, while $N_{\ell+1}$ is increased, beyond N_ℓ , in order to lower the final temperature $T = T_{\ell+1}$.¹⁹ This last, $(\ell + 1)$ -th step is repeated with several different values of $N_{\ell+1}$, in order to scan the low- T regime.

The s -wave T_c is then determined by interpolation between two adjacent low- T points, T_+ and T_- , say, which bracket the instability, that is, their pairing eigenvalues, $\lambda(T_+) < 1 < \lambda(T_-)$, bracket unity. The s -wave transition temperatures estimated from the three different calculations are $T_c/t = 0.093, 0.090$, and 0.091 for $\ell = 3, 4$, and 5 , respectively. Thus, both the T_c and the $\lambda(T)$ results [Fig. 7] obtained with the three different lower cutoff protocols, $\ell = 3, 4, 5$, are in excellent ($\sim 1 - 2\%$) agreement.

For all further T_c results discussed below, the same “factor-2 plus fixed- Ω_ℓ ” NRG protocol is used, with an initial temperature $T_0/t = 4.0$, initial cutoff $\Omega_0/t = 100.5$, and $\ell = 5$ of factor-2 NRG steps, corresponding to $T_\ell/t = 0.125$ and a lower cutoff $\Omega_\ell/t = 3.142$.

Fig. 8 shows the s -wave T_c as a function of the EP coupling strength U_p . A 16^2 grid is employed. The Einstein phonon frequency is $\Omega_p = 1.0t$. Within the FLEX approximation, the s -wave T_c of the Holstein model increases with U_p over a wide range of the EP coupling and saturates when the U_p is comparable to the band width ($8t$).

The finite size effect at the low temperatures needs to be treated carefully. We therefore

calculate the s -wave transition temperature as a function of electron concentration $\langle n \rangle$ in a wide filling range near half-filling. The results are shown in Fig. 9 for three different \mathbf{k} -grids, $N = 16^2$, 32^2 , and 64^2 . The 16^2 grid gives reasonable estimates over for a wide temperature range, down to the lowest temperatures we reach in the calculation, $T \sim 0.02t$. A 32^2 grid, in general, covers this whole temperature range, down to $0.02t$ very accurately.

Three sets of s -wave T_c are reported here corresponding to an on-site Coulomb $U/t = 0$ (Holstein model), 2, and 3. All of them have the same Einstein phonon frequency $\Omega_p/t = 1.0$ and EP coupling $U_p/t = 4.0$. The presence of the on-site Coulomb repulsion suppresses the s -wave pairing and T_c goes to zero or becomes smaller than our lowest numerically accessible T ($\sim 0.02t$), when U approaches U_p . Thus, in essence, T_c goes to zero (or a numerically “very small” value) when the on-site Coulomb repulsion U overcomes the phonon-mediated on-site attraction U_p . Note that there is no significant reduction of the s -wave-supressing U effect due to retardation, that is, due to the “pseudo-potential” reduction of the Coulomb repulsion.^{28,29} This is perhaps not surprising, since, on the one-hand, the phonon-frequency is quite sizeable here, compared to the band-width $8t$, and, on the other hand, near 1/2-filling there may be relevant electronic (charge, spin, and/or pair) flucutation energy scales in the problem which are even closer to the phonon energy scale. Note also that, there exists an “optimal” doping, of about 20% to 30%, where a maximum s -wave transition temperature T_c occurs for this model in the FLEX approximation.

A comparison between FLEX and conventional Eliashberg theory in the s -wave pairing regime $U < U_p$, is shown in Fig. 10. Here, we have used the bare potential $U + v_p(i\omega_n - i\omega_{n'})$ as the effective exchange potential in the self-consistent (Migdal) self-energy calculation and as the pairing potential V_{pair} in the Eliashberg pairing eigenvalue calculations. Thus, in essence, our Eliashberg calculation negelects all the screening effects due to electronic particle-hole and particle-particle fluctuations which the FLEX approximation seeks to include. At sufficiently large doping, $\gtrsim 15 - 20\%$, where converged results for T_c can be obtained in both approaches, the FLEX T_c is noticeably higher than the Eliashberg T_c . This suggests that the predominant (*i.e.*, charge) fluctuations included in FLEX enhance the

s-wave pairing potential. Because of the lack of screening in the Eliashberg (and because of its presence in the FLEX) calculation, it is not surprising that the relative discrepancy between the two approaches becomes even larger in the presence of a finite on-site $U = 2.0t$, as shown by the dashed line results in Fig. 10.

A physically very interesting problem to study in the Holstein–Hubbard model is the competition between *d*– and *s*–wave singlet pairing. While the $d_{x^2-y^2}$ pairing instability is by now well-established in several high- T_c cuprates, there is also mounting (although by no means unambiguous) experimental evidence for *s*–wave pairing in some of these materials.^{2,36} On the theoretical side, it is, within a weak-coupling self-consistent diagrammatic framework, well-established that a $d_{x^2-y^2}$ pairing instability can be driven, or at least enhanced by AF SF exchange,^{3–8} while being suppressed, due to self-energy effects, by the presence of phonon exchange^{14,15}. An *s*–wave instability, on the other hand, can be driven or enhanced by phonon exchange, while being suppressed by AF SF exchange and local Coulomb repulsions, as already discussed above. Thus the two possible candidate pairing mechanism for *d*– and *s*–wave pairing tend to be mutually destructive.

The Holstein–Hubbard model, treated in the FLEX approximation, may be a reasonable starting point to investigate the magnitude these mutually destructive “anti-pairing” effects, both on the *s*–wave and on the *d*–wave side of the phase boundary. In Fig. 9(a) and (b), we plot the *s*– and, respectively, *d*–wave phase diagram at a fixed $U_p = 4.0t$ and, respectively, fixed $U = 4.0t$, for on-site Coulomb repulsions $U/t = 0, 2$ and 3 , and respectively, for on-site attraction $U_p/t = 0, 2$ and 3 . The Einstein phonon frequency is fixed at $\Omega_p/t = 0.5$ for both cases. In comparing the two pairing states, we note that the *s*–wave state which has the higher T_c in the absence of its “anti-pairing” interactions ($U = 0$) is also suppressed more strongly, when its anti-pairing interaction U is turned on. We note also that the *s*–wave instability exists over a wider range of doping $1 - \langle n \rangle$. An optimal doping with very broad T_c maxima is found in both *s*– and *d*–wave pairing states. In the *s*–wave case this occurs at 20% to 30% hole dopings, depending on the on-site Coulomb repulsion U/t ; in the *d*–wave case the T_c -maximum is near 10% doping with a much less pronounced dependence on U_p .

Another important feature to study in the Holstein–Hubbard model is the isotope effect, that is, the dependence of the superconducting T_c on the isotopic mass M of the ions. In our parametrization of the model, this isotopic mass dependence enters only via the Einstein phonon frequency Ω_p , that is, via Eq. (2), since all other parameters (t, U, C, K, U_p) are of purely electronic origin, *i.e.*, not dependent on M . An important experimental measure of the lattice effects on T_c is the isotope exponent

$$\alpha = -\frac{\partial \ln T_c}{\partial \ln M} \Big|_e = \frac{1}{2} \frac{\partial \ln T_c}{\partial \ln \Omega_p} \Big|_e , \quad (44)$$

where the notation $\dots|_e$ means that the partial derivative should be taken with all above-identified electronic parameters held constant. The second equality in (44) follows from Eq. (2).

In Fig. 12, we plot both the s – and d –wave superconducting transition temperatures as a function of the phonon frequency Ω_p . In the s –wave case, Fig. 12(a), T_c rises approximately linearly with Ω_p , up to Ω_p of about $2 - 3t$. At larger Ω_p , T_c gradually becomes sub-linear and approaches saturation which is reached when Ω_p becomes of the order of the electronic bandwidth, that is, in physical terms, unrealistically large. The linear Ω_p -dependence of the s –wave T_c implies that the isotope exponent is given essentially by its classical BCS value for conventional phonon-mediated s –wave superconductivity,

$$\alpha \cong \frac{1}{2} , \quad (45)$$

in the physically relevant low- Ω_p regime $\Omega_p \lesssim t/4$.

In the d –wave case, T_c has only a very weak, slightly decreasing Ω_p dependence. The d –wave isotope exponent is therefore negative and small in magnitude, typically with

$$|\alpha| < 0.05 \quad (46)$$

in the physically realistic Ω_p -regime $\Omega_p \lesssim t/4$. This is much smaller than typical orders of magnitudes $|\alpha| \sim 0.4 - 1.0$ observed in non-optimally doped cuprates, but confirms the conclusions from earlier calculations of the isotope exponent due to harmonic phonon exchange in diagrammatic d –wave pairing models.^{14,35}

V. SUMMARY

In summary, we have developed an important generalization of the numerical renormalization group (NRG) technique for solving the self-consistent field equations of the fluctuation exchange (FLEX) approximation in the presence of a phonon-mediated, retarded bare interaction potential. In the presence of retarded bare interactions neither fast Fourier transform¹⁷ nor the previously developed NRG approach^{20,19} for purely instantaneous interactions can be employed. On the other hand, our generalized “fermion frequency matrix” NRG technique, produces large gains in computational efficiency, both in terms of CPU time and in terms of memory requirements, relative to a brute force calculational approach.

In the physically most interesting low temperature regime, the CPU time and memory requirements of the brute force approach exceed by far the limits of currently available computational resources. By contrast, our generalized NRG method yield efficient, accurate solutions and allows detailed studies of superconducting instabilities in this regime, down to temperature scales 3 orders of magnitude below the electronic bandwidth. Our work also suggests possible avenues towards solving more complicated self-consistent approximation schemes, such the parquet approximation^{5,30}.

We have tested and applied this NRG approach in the context of the FLEX approximation to the the 2D Holstein–Hubbard model. In this model, the FLEX equations are simplified due to the lack of momentum (\mathbf{q} -) dependence in the bare Coulomb and in the bare phonon-mediated interaction potentials. However, more general electron-phonon interaction models, including \mathbf{q} -dependent potentials can easily be accommodated in our NRG approach, by combining it with computationally efficient real-space basis representations^{23,24,34}. Such real-space basis representations have recently been implemented with great success to solve the FLEX equations in extended Hubbard model systems with instantaneous, but \mathbf{q} -dependent bare interaction potentials.

By varying the on-site Coulomb repulsion and EP coupling strength we have studied the competing s – and d –wave superconducting instabilities of the 2D Holstein–Hubbard

model in the FLEX approximation. An optimal T_c for both cases was observed at about 20% to 30% doping for s -wave pairing and 10% for d -wave pairing. The s -wave phase is favored when the phonon-mediated on-site attraction U_p exceeds the on-site Coulomb repulsion U and its transition temperature is suppressed by increasing U . Likewise, the d -wave phase is favored when the on-site Coulomb repulsion U exceeds the phonon-mediated on-site attraction U_p and its transition temperature is suppressed by increasing U_p . When $U \sim U_p$, the T_c 's of both pairing states are suppressed to zero or to a numerically inaccessible very-low temperature regime.

Finally, the isotope exponent α for the s -wave state is BCS like, that is, $\alpha \cong \frac{1}{2}$, at realistic phonon frequencies $\Omega_p/t \lesssim 0.25$. In the d -wave state, the isotope exponents are negative and small in magnitude, with typically $|\alpha| < 0.05$ in the physical phonon frequency regime $\Omega_p/t \lesssim 0.25$. The overall magnitude of α is far too small to explain observed isotope data in non-optimally doped cuprates. Our full FLEX results thus support the conclusions of earlier d -wave isotope calculations by the present authors.^{14,15,35}

We would like to thank Prof. N.E. Bickers for many helpful discussions. This work was supported by the National Science Council (NSC, Taiwan, R.O.C.) under Grant Nos. 872112-M194011 and 882112-M194001 (C.-H. P.), by the U. S. National Science Foundation under Grant No. DMR-9215123 (H.-B. S.) and by computing support from UCNS, University of Georgia, and National Center for High-Performance Computing (NCHC, Taiwan, R.O.C.) are gratefully acknowledged.

REFERENCES

- ¹ For a review of the experiments, see D. J. van Harlingen, Rev. Mod. Phys. **67**, 515 (1995); and references therein.
- ² For an overview of experimental and theoretical aspects, see D.J. Scalapino, Physics Reports **250**, 329 (1995); B.G. Levi, Physics Today **46**, No.5, 17 (1993); and references therein.
- ³ N.E. Bickers, D.J. Scalapino and R.T. Scalettar, Int. J. Mod. Phys. B **1**, 687 (1987).
- ⁴ N.E. Bickers and D.J. Scalapino, Ann. Phys. (N.Y.) **193**, 206 (1989).
- ⁵ N.E. Bickers and S.R. White, Phys. Rev. B **43**, 8044 (1991).
- ⁶ K. Yonemitsu, J. Phys. Soc. Jpn. **58**, 4576 (1989).
- ⁷ T. Moriya, Y. Takahashi, and K. Ueda, J. Phys. Soc. Jap. **59**, 2905 (1990); K. Ueda, T. Moriya, and Y. Takahashi, in *Electronic Properties and Mechanisms of High-T_c Superconductors*, eds. T. Oguchi *et al.*, pp. 145 (North-Holland, 1992).
- ⁸ A. Millis, H. Monien, and D. Pines, Phys. Rev. B **42**, 167 (1990); P. Monthoux, A. V. Balatsky, and D. Pines, Phys. Rev. Lett. **67**, 3448 (1991); Phys. Rev. B **46**, 14803 (1992); P. Monthoux and D. Pines, Phys. Rev. Lett. **69**, 961 (1992); Phys. Rev. B **47**, 6069 (1993); *ibid.* **49**, 4261 (1994).
- ⁹ M.K. Crawford *et al.*, Phys. Rev. B **41**, 282 (1990); Science **250**, 1390 (1990).
- ¹⁰ J.P. Franck *et al.*, Physica C **185-189**, 1379 (1991); Phys. Rev. Lett. **71**, 283 (1993); J. P. Franck and D. D. Lawrie, Physica C **235-240**, 1503 (1994);
- ¹¹ For a review, see J.P. Franck, in *Physical Properties of High-T_c Superconductors IV*, ed. by D.M. Ginsberg (World Scientific, 1994), p. 189; and references therein.
- ¹² J.P. Franck *et al.*, J. Supercond. **8**, 591 (1995); J. P. Franck, Physica Scripta **T66**, 220 (1996).

¹³ For reviews see *Lattice Effects in High- T_c Superconductors*, Y. Bar-Yam, T. Egami, J. Mustre-de Leon, and A. R. Bishop (eds.) (World Scientific, Singapore, 1992); S.J.L. Billinge *et al.*, in *Strongly Correlated Electronic Materials: The Los Alamos Symposium 1993*, K. Bedell *et al.* (eds.) (Addison-Wesley Reading, Massachusetts, 1994); T. Egami and S. J. L. Billinge, Prog. Mater. Sci. **38**, 359 (1994); T. Egami and S. J. L. Billinge, in *Physical Properties of High Temperature Superconductors V*, D. M. Ginsberg (ed.) (World Scientific, Singapore, 1996); and references therein.

¹⁴ H.-B. Schüttler and C.-H. Pao, Phys. Rev. Lett. **75**, 4504 (1995).

¹⁵ C.-H. Pao and H.-B. Schüttler (to be published).

¹⁶ G. Baym and L.P. Kadanoff, Phys. Rev. **124**, 287 (1961); G. Baym, *ibid.* **127**, 1391 (1962).

¹⁷ J.W. Serene and D.W. Hess, Phys. Rev. B **44**, 3391 (1991); J. Phys. Chem. Solids **52**, 1385 (1991).

¹⁸ John Luo and N.E. Bickers, Phys. Rev. B **47**, 12153 (1993); *ibid.* **48**, 15983 (1993).

¹⁹ C.-H. Pao and N.E. Bickers, Phys. Rev. B **49**, 1586 (1994).

²⁰ C.-H. Pao and N.E. Bickers, Phys. Rev. Lett. **72**, 1870 (1994); P. Monthoux and D.J. Scalapino, *ibid.* 1874 (1994); T. Dahm and L. Tewordt, *ibid.* **74**, 793 (1995).

²¹ St. Lenck, J.P. Carbotte, and R.C. Dynes, Phys. Rev. B **50**, 10149 (1994).

²² C.-H. Pao and N.E. Bickers, Phys. Rev. B **51**, 16310 (1995).

²³ G. Esirgen and N. E. Bickers, Phys. Rev. B **55**, 2122 (1997); *ibid.* **57**, 5376 (1998).

²⁴ G. Esirgen, H.-B. Schüttler, and N. E. Bickers, cond-mat/9806264.

²⁵ F. Marsiglio, Physica C**160**, 305 (1989); Phys. Rev. B**42**, 2416 (1990); J. Low Temp. Phys. **87**, 659 (1992).

²⁶ A.B. Migdal, Zh. Eksp. Teor. Fiz. **34**, 1438 (1958); [Sov. Phys. JETP **7**, 996 (1958)].

²⁷ G.M. Eliashberg, Zh. Eksp. Teor. Fiz. **38**, 966 (1960) [Sov. Phys. JETP **11**, 696 (1960)].

²⁸ See, e.g., D.J. Scalapino, in *Superconductivity*, ed. R.D. Parks (Marcel Dekker, New York, 1969), Vol. 1.

²⁹ P.B. Allen and B. Mitrovic, in *Solid State Physics*, ed. by H. Ehrenreich, F. Seitz, and D. Turnbull (Academic Press, New York, 1982), Vol 37, pp.1-91.

³⁰ C. de Dominicis and P.C. Martin, J. Math. Phys. **5**, 14, 31 (1964).

³¹ N.E. Bickers, *Numerical Methods for Lattice Quantum Many-Body Problems* (Addison-Wesley, Reading, MA, in press).

³² J. Zhong and H.-B. Schüttler, Phys. Rev. Lett. **69**, 1600 (1992).

³³ J.K. Freericks and M. Jarrell, Phys. Rev. Lett. **75**, 2570 (1995).

³⁴ W. Hanke and L. J. Sham, Phys. Rev. Lett. **33**, 582 (1974); Phys. Rev. B **12**, 4501 (1975).

³⁵ C.-H. Pao and H.-B. Schüttler, Phys. Rev. B **57**, 5051 (1998).

³⁶ For recent reviews, see J. F. Annett, N. D. Goldenfeld, and A. J. Leggett, in *Physical Properties of High Temperature Superconductors V*, D. M. Ginsberg (ed.) (World Scientific, Singapore, 1996); R. Gatt and P. Chaudhari, Superlatt. Microstruct. **23**, 945 (1998); and references therein.

FIGURES

FIG. 1. (a) The bare interactions in the Holstein–Hubbard model, which include the on-site Coulomb repulsion U and the EP coupling $v_p(i\nu_m)$. (b)–(d) show the bare vertices of the Holstein–Hubbard model in FLEX approximation. These diagrams include contributions (b) V^D from density, and (c) V^M from magnetic particle–hole fluctuations as well as (d) V^S from singlet and V^T from triplet particle–particle fluctuations. In (d), the upper (+) sign pertains to V^S , the lower (−) sign to V^T .

FIG. 2. Imaginary frequency discretization for the frequency NRG space. (a) Initial stage of the frequency space with cutoff Ω_0 , including four positive and four negative fermion frequencies, corresponding to $N_0 = 4$. (b) After one “factor-2” NRG operation, the lower cutoff is $\Omega_1 = \Omega_0/2$. There are eight frequencies in “ L_1 ” and four frequencies in “ H_1 ”. (c) After two “factor-2” NRG operations, the lower cutoff becomes $\Omega_2 = \Omega_0/4$. There are 8 frequencies in “ L_2 ” and eight frequencies in “ H_2 ”.

FIG. 3. Imaginary part of self-energy $\Sigma(k) = \Sigma_1(k) + i\Sigma_2(k)$ and Green’s function $G(k)$ for a brute force calculation at four different temperatures: $T/t = 1.0$ (cross symbols), 0.5 (squares), 0.25 (circles), and 0.125 (lines) at $\mathbf{k} = (1.77, 1.77)$. (a) Real part of self-energy Σ_1 . (b) Imaginary part of self-energy Σ_2/ω_n (c) The real part (solid symbols and line) and imaginary part (open symbols and dashed line) of G . The parameters are: $\Omega_0 = 25t$, $U/t = 0$, and $\langle n \rangle = 1.0$.

FIG. 4. The same parameters as in Fig. 3 with the $\mathbf{k} = (2.95, 0.20)$, which is right at the Fermi surface. Plots are shown for imaginary parts of self-energy and Green’s function only; the real parts of self-energy and Green’s function vanish on the Fermi surface at $\langle n \rangle = 1.0$, due to particle-hole symmetry.

FIG. 5. Comparison of the self-energy [(a) for real part and (b) for imaginary part] and Green’s function [(c) solid line for real part and dashed lines for imaginary part] using factor-2 frequency NRG and a brute force approach. Results from 3 stages of NRG are represented by symbols. Results from brute force are represented by lines. The parameters are the same as Fig. 3.

FIG. 6. Comparison of (a) the self-energy and (b) Green's function using factor-2 frequency NRG and a brute force approach. Results from 3 stages of NRG are represented by symbols. Results from brute force are represented by lines. The parameters are the same as Fig. 4

FIG. 7. Maximal eigenvalue λ_s of the pairing kernel Eq. (22) in the s -wave symmetry channel for three different lower cutoffs: $\Omega_\ell/t = 12.56$ (solid line); 6.283 (cross symbols), and 3.142 (open circles). The model parameters are: $\Omega_p/t = 5.0$, $U_p/t = 4.0$, $U/t = 2.0$, and $\langle n \rangle = 0.75$

FIG. 8. The s -wave transition temperature T_c as a function of the EP coupling strength U_p for the Holstein model ($U = 0$) with Einstein phonon frequency $\Omega_p/t = 1.0$ and electron filling factor $\langle n \rangle = 0.75$.

FIG. 9. Phase diagrams for the s -wave superconductivity of the Holstein–Hubbard model for different on-site Coulomb repulsion. The model parameters are $U_p/t = 4.0$ and $\Omega_p/t = 1.0$. The on-site Coulomb repulsion $U/t = 0, 2.0, 3.0$ (from the top curve to the bottom one). Three different \mathbf{k} -grid sizes are employed.

FIG. 10. Comparison of Eliashberg (open squares) and FLEX (open circles) solution for the phase diagrams for the s -wave superconductivity of Holstein–Hubbard model. The parameters are the same as Fig. 9 but data are shown only for $U/t = 0$ (solid lines) and 2 (dashed lines).

FIG. 11. Superconducting phase diagram of the Holstein–Hubbard model for (a) s -wave pairing with $U_p = 4.0t$ and several different U (b) d -wave with $U = 4.0t$ and several different U_p .

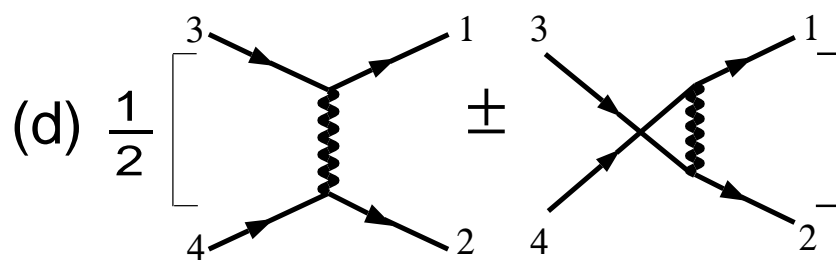
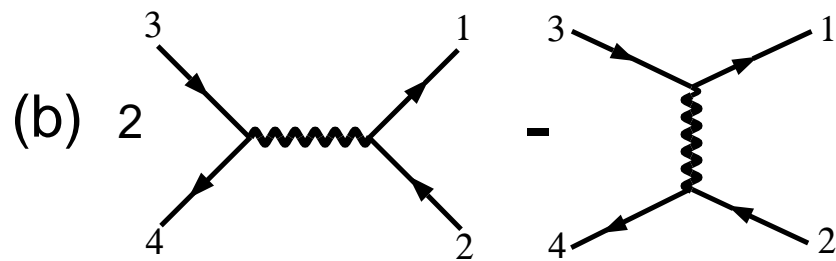
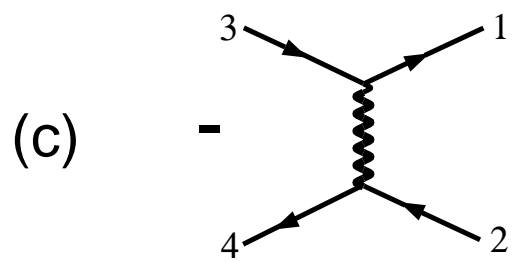
FIG. 12. (a) s -wave and (b) d -wave transition temperatures T_c as functions of the Einstein phonon frequency Ω_p near the optimal doping ($\langle n \rangle = 0.75$ for s -wave and 0.90 for d -wave). In (a), $U_p/t = 4.0$ and $U/t = 0$ (solid line) and $U/t = 2.0$ (dashed line). In (b), $U/t = 4.0$ and $U_p/t = 2.0$.

TABLES

TABLE I. Comparison of memory and CPU time requirements between brute force and frequency NRG calculations. Parameters are the same as in Fig. 5. The calculations were performed on an IBM RS6000/397 workstation.

	memory	CPU time per iteration
brute force	105 MB	78.1 sec
frequency NRG	9 MB	0.6 sec

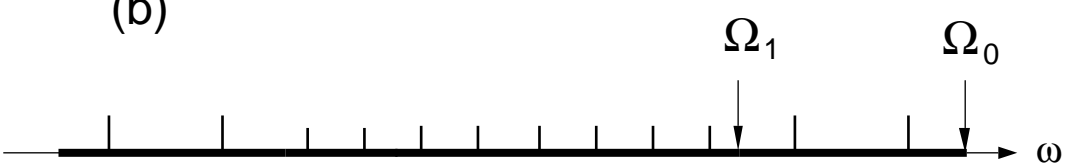
$$(a) \text{---} = \text{---} + v_p(i v_m)$$



(a)



(b)



(c)

